Modal Identification of the Z24 Bridge Using MIMO-AMI

M. S. Allen, and J. H. Ginsberg
The G. W. Woodruff School of Mechanical Engineering
Georgia Institute of Technology
Atlanta, GA 30332-0405

November 15, 2004

Abstract

The Algorithm of Mode Isolation (AMI) employs a strategy in which modes are sequentially identified and subtracted from a set of FRFs. Their natural frequencies, damping ratios and mode vectors are then refined through an iterative procedure. This contrasts conventional multi-degree-of-freedom (MDOF) identification algorithms, most of which attempt to identify all of the modes of a system simultaneously. A mulit-input-multi-output (MIMO) implementation of AMI was presented in a companion paper, and validated using noise-contaminated analytical data. This paper presents the application of MIMO-AMI to experimentally obtained data from MIMO, shaker excited tests of the Z24 highway bridge, demonstrating the algorithm's performance on a data set typical of many EMA applications. Considerations for determining the number of modes active in the frequency band of interest are addressed, and the results obtained are compared to those found by other researchers.

Nomenclature

$H_{jP}(\omega)$	FRF for displacement j due to excitation P	$\{\phi_r\}$	displacement portion of rth mode vector (Normalized)
H_{c}	Composite FRF	$\{q\}$	Generalized coordinates
H_{cn}	Condensed FRF (Nyquist Plots)	w	Transverse displacement
$[A_r]$	Modal residue matrix for the rth mode	θ	Torsional rotation
		ω	Drive frequency
λ_r	rth eigenvalue	N_o	Number of outputs
ω_r	rth natural frequency	N_i	Number of inputs
ζ_r	rth modal damping ratio	α	Peak selection parameter

1 Introduction

In the early days of experimental modal analysis (EMA), modal parameter estimation was typically performed using single-degree-of-freedom (SDOF) methods, such as peak-picking or circle-fitting. SDOF methods gave fairly accurate results, provided that the data was not too noisy and the natural frequencies of the system under test were well separated. However, when modes with close natural frequencies were encountered the methods became inaccurate or failed. As a result, the modal analysis community began to seek simultaneous, multi-degree of freedom (MDOF) approaches. Most MDOF algorithms ignore the frequency-domain decoupling of modes upon which legacy SDOF algorithms depended. Processing all data simultaneously using the MDOF approach often requires the use of high order polynomials, introducing numerical ill-conditioning, as well as increasing the computational effort. In most cases non-physical or computational modes are identified together with the true modes of the system. In order to obtain meaningful results a user must first distinguish the true or physical modes from the spurious ones. This is typically done with the aid of a stabilization diagram, which requires applying the MDOF algorithm at a number of model orders and then searching for those modes that are consistently identified from one model order to the next. Once stable modes are identified, one must also decide which model order yields the most accurate estimates of their modal parameters. This is especially important in condition monitoring or other applications that require

highly accurate estimates of the modal parameters. Furthermore, computationally efficient practices for creating a stabilization diagram can mask inaccuracies in the modal parameters, as shown in [1].

The hybrid, MIMO Algorithm of Mode Isolation (AMI) [2] blends the SDOF and MDOF approaches to provide an alternative to conventional SDOF or MDOF methods. In a companion paper [2], MIMO-AMI was presented and tested on noise contaminated analytical data from two vibratory systems. MIMO-AMI is an MDOF method, in that it accounts for the overlap of all modal contributions, but it identifies a system using SDOF or low order MDOF parameter fitting, exploiting the uncoupling of modal contributions in the frequency domain. MIMO-AMI works by considering each peak in a composite FRF of the MIMO data set in order of dominance, applying either an SDOF fit if a single mode is present, or an MDOF fit if multiple close modes are indicated. In accord with the basic AMI concept, the identified mode(s) are subtracted from the data as they are identified and the procedure continues until the data is reduced to noise. The modes are then isolated in a second stage to account for overlapping modal contributions. This is done by subtracting contributions of all of the modes of the system except for one (or one group of modes associated with a single peak) from the FRF. This leaves only the contribution of either a single mode or a small group of heavily coupled modes, which are re-fit using data around the FRF peak in focus, in order to obtain more accurate estimates of their modal parameters. These updated modal parameters are stored, and the algorithm proceeds through all groups of modes until convergence criteria on the natural frequencies, damping ratios and residues is met.

This simple approach is numerically efficient, so many input and output sensors can be processed simultaneously. Comparisons of AMI with other simultaneous MDOF algorithms [1], [2], [3], [4], such as the data-driven stochastic subspace algorithm (SSI), the poly-reference Least Squares Complex Frequency Domain (pLSCF) algorithm and the Rational Fraction Polynomial algorithm (RFP or Orthogonal Polynomial algorithm OP,) applied to noise-contaminated data have shown that AMI performs favorably. Because AMI is based on a pole-residue representation of the transfer function, there is no theoretical upper limit to the number of modes that can exist in the data set being processed. On the other hand, many frequency domain algorithms are based on a rational polynomial model that is ill conditioned at high model order.

The present work demonstrates the application of the MIMO-AMI algorithm to experimentally derived data, specifically, the data obtained in shaker tests of the Z24 highway bridge in Switzerland. A large quantity of data was taken from this bridge as part of a proof of concept test investigating the feasibility of condition monitoring of civil structures. Data from one of these tests was supplied to various researchers, most of which presented their results at the 19th IMAC conference (1999) [5], [6], [7] and [8]. The following section presents a brief description of MIMO-AMI. In Section 3 the algorithm is applied to FRFs created from the Z24 bridge vibration data. Section 4 offers some conclusions.

2 Hybrid, MIMO Implementation of AMI

The primary concepts of MIMO-AMI will be described here. A more detailed description can be found in [2], wherein the application of the algorithm to analytical test problems was also presented. AMI finds a pole-residue model of the FRF matrix $[H(\omega)]$ described by

$$[H(\omega)]_{N_i \times N_o} = \sum_{r=1}^{N} \left(\frac{[A_r]}{i\omega - \lambda_r} + \frac{[A_r^*]}{i\omega - \lambda_r^*} \right) \quad (1)$$

$$[A_r] = \{\psi_r\} \left\lfloor L_{P_1,r} \ldots L_{P_{N_i},r} \right\rfloor \quad (2)$$

where ω is the frequency, and λ_r and $[A_r]$ are respectively the eigenvalue and residue matrix of the state-space pole-residue model. The eigenvalue is related to the "undamped" natural frequency ω_r and damping ratio ζ_r by: $\lambda_r = -\zeta_r \omega_r \pm i\omega_r \left(1 - \zeta_r^2\right)^{1/2}$. The complex residue matrices returned by AMI have dimensions $N_o \times N_i$, where N_o and N_i respectively denote the number of outputs (or measurement points) and the number of inputs (or drive points.) The residue matrices identified by AMI are rank-one, so they can be decomposed into a mode shape $\{\psi_r\}$ and modal participation factors $\left\lfloor L_{P_1,r} \ldots L_{P_{N_i},r} \right\rfloor$ as shown in eq. (2), where $P_1 \ldots P_{N_i}$ denote the indices of the input or drive points.

A composite FRF, defined as the average of the magnitude of all $N_o N_i$ FRFs, is used for monitoring of the AMI algorithm and display of the data. AMI begins by considering the highest peak in the composite FRF. A user-set parameter selects which data around each peak should be used for parameter identification [2]. This peak data

is processed by a common-denominator, SDOF algorithm which returns the eigenvalue and residue matrix for the mode identified. Use of a common-denominator algorithm results in the identification of a residue matrix which can have a rank greater than one, but no larger than $\min(N_i, N_o)$. This residue matrix is decomposed via singular value decomposition, revealing the rank of the matrix as the number of singular values of magnitude comparable to the first. The relative magnitude of each singular value is described numerically by its singular value ratio SR_k, defined as

$$SR_k = S_k/S_1 \tag{3}$$

where S_k denotes the kth singular value of the residue matrix. When $SR_k \ll 1$ for $k > 1$, indicating that a single mode is present, the residue matrix returned by the common denominator algorithm is reduced to rank one by retaining only the part of the SVD which corresponds to the first singular value. The measured FRF is then compared to an FRF model for the mode, constructed using this rank-one residue and the identified eigenvalue in eq. (1). If the agreement is deemed acceptable, the mode is retained and its FRF model is subtracted from the FRF data forming a set of "subtraction residual" FRF data. The mode subtraction procedure is repeated on the resulting subtraction residual until a composite FRF of the subtraction residual shows no evidence of additional modes, at which point the algorithm proceeds to the isolation stage, described subsequently.

When the peak data contains the response of more than one mode, the number of singular value ratios SR near one reveals the number of modes active at the peak. An MDOF fit of the indicated model order is then performed using a MIMO-MDOF algorithm, which returns the eigenvalues and rank-one residue matrices of the identified modes. (The algorithm used for these MDOF fits is the Frequency-Domain Subspace Algorithm described in [9].) The modal parameters identified by the MIMO-MDOF algorithm are used to create an FRF model for these modes only, which is compared to the residual FRF data. The modal parameters found at the peak in focus are stored and their contributions to the FRFs, found using eq. (1), are subtracted from the residual FRF data, bringing the next highest peak in the composite FRF into dominance. If inadequate agreement is obtained using both SDOF and MDOF methods, the estimated modal parameters are discarded and the subtraction phase either ceases or proceeds to a different peak in the composite FRF.

Two difficulties can arise during this subtraction process. First, the composite FRF of the subtraction residual might show a peak in the frequency interval of a previously identified mode. (Due, for example, to systematic errors in the data, inaccuracy of the modal parameters, or narrow-band noise.) As modes are removed from the data set, this peak may come into dominance again, so that one might erroneously identify additional modes in this frequency band. To avoid this scenario the data within the frequency interval fit by AMI is not included in subsequent searches for additional modes. One can verify that the appropriate number of modes has been identified at each peak after the mode isolation phase, as described subsequently. The second difficulty that can arise is a situation in which all of the singular value ratios SR_k are significant. In this case one does not definitively know the number of modes present at the peak under consideration. The only recourse is to try fitting an increasing number of modes comparing the residual FRF data with reconstructed FRFs for the identified modes at each model order, and then choose the lowest order that results in adequate agreement. This will be demonstrated when processing the Z24 data in the following section.

The steps described in the preceding use a composite FRF to select frequency intervals to be searched for modes. Composite FRFs also are used to compare the subtraction residual FRFs to the FRFs reconstructed from the parameters of the mode(s) under consideration. The use of composite FRFs expedites the assessment because visually examining plots of each individual FRF would be quite tedious. Two types of composites are examined. The magnitude composite, defined previously, is a standard way of displaying FRF data, and provides the first means for comparison. It is also helpful to have a comparison that includes the phase of the responses, such as a Nyquist plot. In [2] the authors proposed a definition for a composite Nyquist FRF, in which the actual FRF data is condensed using the residue matrix $[(A_{\text{fit}})_r]$ of the mode under consideration. The condensed FRF data or "Nyquist composite FRF" $(H_{\text{cn}})_r(\omega)$ is constructed according to

$$(H_{\text{cn}})_r(\omega) = tr\left([(A_{\text{fit}})_r]^H * [X(\omega)]\right) \tag{4}$$

where $tr()$ is the trace operator and $[X(\omega)]$ is the FRF data being condensed. Clearly the Nyquist composite FRF is dependent on the residue matrix used in forming it, and hence is only truly meaningful for a single mode. When multiple modes are identified at a single peak, a composite Nyquist FRF is created for each individual mode. The motive is to evaluate how well the FRFs reconstructed using the parameters of each mode match the measured FRFs. Towards this end, an identified or "fit" FRF model is constructed for each mode using the associated term in eq. (1)

and condensed using eq. (4) resulting in a "fit" Nyquist composite FRF. This is compared to a Nyquist composite FRF of the isolation residual $[(H_{\text{isol}}(\omega))_s]$ for the same mode, defined as follows

$$[(H_{\text{isol}}(\omega))_s] = [H_{\text{meas}}(\omega)] - \sum_{\substack{r=1 \\ r \neq s}} \left(\frac{[A_r]}{i\omega - \lambda_r} + \frac{[A_r^*]}{i\omega - \lambda_r^*} \right) \tag{5}$$

where s is the index of the mode being isolated and $[H_{\text{meas}}(\omega)]$ is the measured set of FRFs. The summation extends over all modes identified. Examples of the comparison between the Nyquist composite of the "fit" FRF and the isolation residual may be seen by considering the figures discussed later, which describe the processing of the Z24 FRF data. For example, the righthand pane in Figure 3 shows Nyquist Composite FRFs of the reconstructed FRFs (dash-dot) and isolation residual (lines) for each of the two modes identified at the peak under consideration. These comparisons are valuable in determining the number of modes contributing at each peak and in deciding when to terminate the subtraction phase, as discussed in the next section.

The modal parameters identified in the subtraction phase do not account for the presence of other modes. Overlapping modal contributions are accounted for by successively isolating each mode or group of modes, and then re-fitting them in the mode isolation stage. The process begins with the dominant peak in the composite FRF. The contributions to each FRF of all modes except for those identified at this peak are subtracted from the original FRF data, forming an isolation residual. This is similar to the isolation residual in eq. (5), although in this case the summation excludes all modes identified at the peak under consideration. This residual then predominantly contains the contributions of the modes in focus. Processing it with the same parameter identification scheme used in the subtraction phase yields better estimates of the mode or modes in focus. Specifically, if the isolation residual contains the contribution of a single mode, the common-denominator SDOF algorithm is used and the resulting residue is reduced to rank-one using the SVD as described previously. When multiple modes are present, the MIMO-MDOF algorithm is used. A cycle through all groups of modes constitutes one iteration. Mode isolation stops when convergence criteria for the eigenvalues and residues have been met.

3 Application to Z24 Bridge Data:

Vibration data from the Z24 bridge in Switzerland shall be used to evaluate the performance of MIMO-AMI. This data is available for download from the Katholieke Universiteit Leuven web-site [14]. A number of researchers analyzed the data and presented their results at the 19th International Modal Analysis Conference, see [5], [6], [7], [10] and [11]. In his thesis [8], Peeters presents a detailed description of the bridge and data sets, as well as a good bibliography of other published results regarding the Z24 bridge. The Z24 bridge was excited by two shakers, one at the mid-span of the bridge and another at a side-span. Because of the size of the bridge, the response was measured in nine setups of up to 15 sensors each, with three response sensors and the two force sensors common to all setups. In each setup, 65,536 samples were collected for each channel with a sampling frequency of 100 Hz. The shakers were driven with uncorrellated random noise, band-limited to 3-30 Hz.

The time histories of the force inputs and acceleration responses for each setup were provided by researchers from KU Leuven. It was necessary to process these time histories in order to estimate MIMO FRFs for the bridge, which could then be processed by AMI. Towards this end, the H_1 estimator was applied to time histories [12] [13]. The data for each setup was divided into 20 blocks of length 4096 samples to which a Hanning window was applied. This resulted in an estimate of the cross spectrum matrix (between the response channels included in the setup and the two force channels) and the auto spectrum matrix (for the force channels), each at 2049 frequency lines. The number of averages used resulted in each record overlapping the previous by approximately 21%. Conforming to standard practice, the H1 estimate of the FRF was then found by post multiplying the cross spectrum matrix with the inverse of the auto spectrum matrix at each frequency line. The same procedure, as well as the windowing and averaging parameters, were used by Schwarz and Richardson [7]. Because three sensors were common to all measurement setups, nine estimates of the FRFs for these sensors were available. These were averaged resulting in an FRF data set with 75 total outputs and two inputs that was processed globally by AMI.

3.1 Subtraction Phase

Figure 1 describes the first subtraction step for the Hybrid MIMO-AMI algorithm. The pane on the left shows the composite magnitude FRF of the Z24 data and a composite magnitude FRF of the fit to the mode found by the SDOF, common-denominator algorithm in the first subtraction step. The frequency points around the peak selected

for the fit using the criteria described in [2] are marked with circles (red). A zoom view is also included in the lower-right corner of the pane highlighting the peak data. The pane on the right displays composite Nyquist FRFs of the data and SDOF fit, both of which were created using the rank-one residue matrix, found by SVD processing the residue matrix returned by the SDOF algorithm.

Figure 1 shows imperfect agreement between the FRF data and the fit, suggesting that a higher order fit might be warranted. However, the second singular value ratio of the residue matrix returned by the common-denominator algorithm corresponds to $SR_2 = 0.0058$. This suggests that a second mode is not present at this peak, so an MDOF fit is not warranted. Experience has shown that it usually is good practice to proceed to identify modes in other frequency intervals when one encounters an uncertain situation such as this. In many cases the discrepancies between the data and the reconstructed FRF are reduced or eliminated after mode isolation. If the discrepancies persist, one can return to the uncertain frequency interval and search for additional modes after mode isolation. For these reasons, a single mode was accepted and subtracted from the FRF data in this step. After removing the fit mode, the data within the frequency band used for finding this mode's parameters was disregarded in all subsequent subtraction steps (assigned a value of zero) to avoid returning to this location until completion of the mode subtraction phase. Note that the disregarded data is not plotted in Figures 2 through 8. After mode isolation, a search for additional modes using the full data set was performed, as described subsequently.

After the single mode found in the first step was removed, the highest peak in the composite magnitude FRF was near 10 Hz. The peak data and resulting SDOF, common-denominator fit are shown in Figure 2. Visual inspection of the composite magnitude plot clearly indicates the presence of at least two modes in this frequency band, which is confirmed by the second singular value ratio being $SR_2 = 0.51$. The result of attempting a two-DOF fit using the MDOF, frequency domain, SSI algorithm is illustrated in Figure 3. In analogy to Figures 1 and 2, the pane on the left shows composite magnitude FRFs of the residual data and the FRF reconstructed using both modes returned by the MDOF algorithm. On the right, two composite Nyquist plots are shown describing the quality of fit of each of the two modes identified in this step. The two modes identified in this peak data set were sorted by ascending natural frequency and have been designated mode 1 and mode 2 in this figure. The mode numbering in each of these figures refers solely to the modes associated with that particular subtraction step. A Nyquist composite of the residual FRF data is compared to a Nyquist composite of the FRF reconstructed for each mode, where the composite for each modal comparison is obtained using the rank-one residue matrix for that mode. Note that the Nyquist composite of the fit FRF and the isolation residual for the second mode where both multiplied by -1 prior to plotting in order to distinguish them visually from those for the first mode. When multiple modes were identified in any of the subsequent subtraction steps, the Nyquist composites for even numbered modes were multiplied by -1 for plotting purposes only. Both the magnitude composite and Nyquist composite plots in Figure 3 show good overall agreement between the data and the fit modes. However, the presence of an additional mode is suggested by the poor agreement between the two peaks in the magnitude composite plot and the irregularity of the Nyquist composite for mode 2. Only two drive points were used in collecting the FRF data, so a third singular value ratio is not available to use as an aide in determining the mode multiplicity in this frequency band. The recourse is to either disregard the differences between the data and fit, or try a three-DOF fit. The result of attempting a three-DOF fit in the frequency band is shown in Figure 4. Modes 1 and 2 fit the residual FRF more poorly than in Figure 3. The third identified mode has a very small damping ratio and residue matrix, and does not contribute noticeably to the composite magnitude FRF. Also, this mode is not visible in the composite Nyquist plot in Figure 4 because the norm of its residue matrix is much smaller than those for modes 1 and 2, though a zoom view reveals poor agreement with the data. For these reasons, the results of attempting to fit three modes to the peak were disregarded, and the two modes found using a 2-DOF fit were retained and subtracted from the data.

The third subtraction step focused on the double peak near 18 Hz. As was the case in the previous step, it was clear that at least two modes were present at this peak. The SDOF fit, for which the second singular value ratio is $SR_2 = 0.52$, is shown in Figure 5. A 2-DOF fit was attempted as shown in Figure 6. Composite Nyquist plots for the two resulting modes agree fairly well with the data, althought the composite magnitude FRF shows that the second mode underestimates the data uniformly. This suggests that the second peak might be due to more than one mode. Furthermore, subtracting the fit 2-DOF FRF from the FRF data shows a residual of considerable magnitude in this region (not shown). For these reasons, three modes were fit to the peak data as shown in Figure 7. Two modes were identified near 19 Hz, both showing good agreement between the Nyquist composite of the data and their reconstructed FRFs. The composite magnitude FRF of the reconstruction using these three modes also shows good agreement with the data, so a higher order fit is not warranted.

The remaining peaks were processed using logic similar to that described for the first three subtraction steps. In steps four and five, two modes were identified at each of the peaks near 12 and 25 Hz, indicated by singular value ratios of $SR_2 = 0.085$ and 0.31 respectively. Despite the relatively small singular value ratio for the pair of modes near 12 Hz, visual inspection of the composite plots provided motivation for searching for an additional mode at this location. The sixth subtraction step is shown in Figure 8, in which an SDOF fit to the data near 5 Hz resulted in a good fit with a singular value ratio $SR_2 = 0.030$. Consequently, this mode was accepted and subtracted from the FRF data, resulting in a total of eleven modes identified. The composite magnitude FRF of the residual, formed by subtracting the contributions of these eleven modes, exhibited no peaks other than those to which previously identified modes have been fit, so the subtraction phase ended with eleven identified modes.

3.2 Isolation Phase

Mode isolation halted after four iterations, at which point the maximum change in any eigenvalue or any element of the residue matrices was less than 0.001%. The composite residual FRF, formed by subtracting the contributions of all identified modes, is shown in Figure 9. The maximum amplitude of the composite of the residual is almost an order of magnitude less than the composite of the original data. Small peaks remain in the vicinity of 4, 5, 10, and 18 Hz, each corresponding to a frequency region already processed by AMI. In general, data remaining above the noise floor in the vicinity of a previously identified modes suggests the presence of either additional modes in the frequency band or systematic errors in the data. In order to verify that no more modes could be extracted in each of these frequency bands, each was searched for additional modes by restoring the contributions of the modes previously identified in the band and then augmenting the order of the fit. An example of this is shown in Figure 10 where four modes are fit to the peak near 18 Hz, at which three modes had been previously identified. The fourth identified mode contributes negligibly to the response, suggesting that only three modes are active in this frequency band. These three modes were retained, and the other peaks were then searched for more modes. Attempting a 2-DOF fit at the peak near 4 Hz even though the singular value ratio was small resulted in no better agreement than that shown in Figure 1, so the single mode identified in this region was retained. No additional modes were identifiable at any of the remaining peaks, so the identification process terminated with eleven modes identified.

Figure 11 shows composite Nyquist FRFs for modes 7-9 after mode isolation. Composite Nyquist plots for these modes before mode isolation were shown in the right pane of Figure 7. Comparison of Figures 11 and 7 illustrates the improvement in the agreement obtained as a result of mode isolation. The agreement in Figure 11 was typical of all of the identified modes except mode 11. Mode 11 was identified concurrently with mode 10 in the frequency band near 25 Hz. Figure 12 shows composite Nyquist plots for modes 10 and 11 after mode isolation and refinement. The scale of the plots illustrates the relative amplitude of the two modes. The contribution of mode 11 is about 20 times smaller than that of mode 10. This is also evidenced by the fact that mode 11 has a smaller residue vector and larger damping ratio than mode 10. The relative unimportance of mode 11 to the response leads one to question the validity of this mode, though there were a number of reasons for retaining it. The singular value ratio at this peak was $SR_2 = 0.32$, suggesting that a second mode was present. (This information should be interpreted with caution, because the upward trend in the composite magnitude plot in this region suggests that out of band modes might be contributing to the rank of the FRF matrix at this location.) Also, the composite magnitude FRF of the subtraction residual showed a coherent peak in this frequency band when only one mode was subtracted. This peak was completely obliterated when two modes were accepted in the frequency band. This observation provided the primary motivation for retaining two modes in this frequency band. In an alternate trial not reported here, MIMO-AMI was applied to the Z24 data for frequencies from 3 to 45 Hz. Because the excitation to the bridge was band limited to 3-30 Hz, it was difficult to extract modes from the FRFs above 30 Hz, although mode 11 was identified once again. Furthermore, even better agreement was found between the fit and reconstructed FRF for mode 11 once the contributions of some of the modes above 30 Hz were removed from the data set.

Figure 13 shows a composite FRF of the Z24 bridge data, a composite of AMI's reconstructed FRFs and a composite of the difference between the two. The fit agrees well with the data, with the most notable discrepancies in the previously mentioned frequency bands. The natural frequencies found by AMI after mode isolation are shown in Tables 1 and 2. The natural frequencies and damping ratios reported by Marchesiello et al [5], Luscher et al [6] and Schwarz and Richardson [7] are also presented in Tables 1 and 2. Some of the aforementioned researchers presented the results of analyzing other data sets taken from the bridge, though only the results for the shaker-excited data sets are shown here. Marchesiello et al [5] processed the bridge data using a covariance driven SSI algorithm, processing the data globally setup by setup, so that no more than 15 responses were processed simultaneously. This approach yields nine estimates for each eigenvalue. The natural frequencies and damping ratios shown in Tables 1

Natural Frequency: Hz, (σ Hz)				
Mode	**MIMO-AMI**	**Marchesiello et al [5]**	**Luscher et al FDD2 [6]**	**Schwarz & Richardson [7]**
1	3.8726	3.85 (0.01)	3.85	3.872
2	4.8246	4.83 (0.02)	4.81	4.821
3	9.7715	9.74 (0.02)	9.72	9.795
4	10.488	10.46 (0.05)	-	10.489
5	12.416	12.31 (0.07)	12.62	12.403
6	13.204	13.31 (0.17)	-	13.086
7	17.344	17.25 (0.18)	-	17.259
8	19.273	19.24 (0.12)	-	19.207
9	19.542	20.24 (0.16)	19.56	-
10	26.656	26.46 (0.07)	26.65	26.665
11	28.122	-	-	-

Table 1: Natural frequencies for Z24 bridge drop test data from various researchers. Standard Deviations are shown in parenthesis for non-global methods.

Damping Ratio: %, (σ %)			
Mode	**MIMO-AMI**	**Marchesiello et al [5]**	**Luscher et al FDD2 [6]**
1	0.95936	1.15 (0.23)	1.08
2	1.7152	1.70 (0.17)	2.19
3	1.5145	1.70 (0.13)	2.13
4	2.1135	1.79 (0.23)	-
5	3.0787	2.75 (0.89)	5.60
6	4.015	3.61 (1.25)	-
7	4.6173	3.26 (2.48)	-
8	2.6387	2.32 (0.30)	-
9	5.7951	1.97 (1.24)	4.67
10	3.1221	2.57 (0.44)	5.15
11	6.7616	-	-

Table 2: Damping Ratios for Z24 bridge drop test data from various researchers. Standard deviation reported in parenthesis for non-global methods.

and 2 for Marchesiello et al are apparently the average of those obtained in nine trials. The associated standard deviation is shown in parenthesis. Luscher et al used the Frequency Domain Decomposition (FDD) algorithm and the Eigensystem Realization Algorithm (ERA) to process the shaker data. They reported that better results were obtained by the FDD algorithm. The results presented in Tables 4 and 5 for Luscher et al are the result of the FDD algorithm applied globally to the data from all setups, denoted the 'FDD2' results in [6]. Schwarz and Richardson used a 'peak cursor' to find the natural frequencies and mode shapes from the drop-test data, processing each setup independently. They did not present damping ratios.

The results for most of the modes are comparable between the algorithms. Most of AMI's natural frequencies and damping ratios fall within a 95% confidence interval of the values presented by Marchesiello et al. Marchesiello et al found an additional mode at 7.9 Hz when processing the shaker data set. However, they attributed it to coloring of the input spectrum, so it was not included in Tables 1 and 2. Luscher et al failed to identify a number of modes found by the other researchers. Only AMI has identified the 11th mode, which is near the high frequency limit of the excitation spectrum.

The mode shapes are displayed in Figure 14. Complex mode vectors were obtained from AMI in accord with the state space description in eq. (1). In order to plot the mode shapes, the real displacement response in each mode was found at the instant when it is an overall maximum. This was accomplished by multiplying each mode shape $\{\psi\}$ by $e^{i\theta}$, with θ found to maximize the realness of the the product $\{\psi\}\, e^{i\theta}$, and then plotting the real part of $\{\psi\}\, e^{i\theta}$. The imaginary part of $\{\psi\}\, e^{i\theta}$ was generally much smaller, indicating that most of the modes had good modal phase collinearity [12]. Modes 7, 9 and 11 were an exception, having fair to poor modal phase collinearity. Modes 1, 5, 6, 9 and 11 consist primarily of bending of the bridge in the vertical direction. The motion of the piers and the number of half-sines along the length of the bridge both increase with mode number. Modes 3 and 4 primarily exhibit bending in the side span with torsion and bending in the main span. These modes are very similar, the primary difference being that the two side spans move out of phase in Mode 3, while they move in phase in Mode 4. Mode 2 shows coupled torsion and side-to-side sway. Modes 7, 8, and 10 are primarily torsional modes having respectively four, five and six nodes along the length of the bridge.

4 Conclusions

Data from the Z24 highway bridge was processed using a hybrid, MIMO implementation of the Algorithm of Mode Isolation (AMI). AMI found the lowest eleven modes of the bridge without the use of a stabilization diagram. Instead modes were successively identified and subtracted from the experimental data until no additional regions were found in which a reasonable fit could be obtained. Particular attention was devoted to identifying modes whose natural frequencies differ by much less than their bandwidths. A metric reflecting the rank of the FRF matrix in a frequency band around a resonance peak provides a guide-line for the user regarding the number of modes needed to fit that peak. In some cases, fits of increasing order were attempted, and the agreement between the data and reconstructed FRFs for the modes fit was evaluated, in order to determine the number of modes that resulted in the best results without including modes of dubious validity. The composite magnitude FRF and the composite Nyquist FRF, defined herein, were found to be extremely helpful in comparing the experimental FRFs with reconstructed FRFs for the identified modes.

In the subtraction phase of the AMI algorithm, two regions were encountered in which two peaks were clearly visible in the composite magnitude FRF. In each case the algorithm that automatically selects the frequency band surrounding each peak in the composite FRF (described in [2],) selected a band encompassing two close peaks. As a result, the modes in each of these frequency bands were identified simultaneously using the MDOF algorithm. The modes identified at these peaks were separated by more than their average half-power bandwidths, and hence could have been treated individually. This would have been preferred because it lessens the order of the parameter identification used in each frequency band. In an alternate trial not presented here, these modes were treated individually resulting in somewhat better agreement between the measured and reconstructed FRFs in the vicinity of modes 7 through 9, though the identified modal parameters were similar.

The natural frequencies and mode shapes of the Z24 bridge that were identified by AMI were found to be comparable to those presented by other researchers. Several of these researchers [8], [5], [11] processed individual patches of the experimental data independently in order to limit the computational burden, resulting in an analysis that was not truly global. The AMI algorithm was capable of globally processing all of the FRFs of the system without requiring excessive computer resources. Furthermore, the AMI algorithm resulted in the identification of an eleventh mode at the upper frequency limit of the FRF data. Though weakly excited, a composite Nyquist plot for this mode showed fair agreement. Furthermore, this mode's shape is similar to what might be expected for the next highest bending mode of the bridge based on simple theory.

ACKNOWLEDGEMENT

This research was supported in part by a National Science Foundation, Graduate Research Fellowship.

References

[1] Matthew S. Allen and Jerry H. Ginsberg, "SIMO extension of the algorithm of mode isolation," in *IMAC 22 - XXII International Modal Analysis Conference*, Dearborn, Michigan, 2004.

[2] Matthew S. Allen and Jerry H. Ginsberg, "Global, hybrid, MIMO implementation of the algorithm of mode isolation," in *23rd International Modal Analysis Conference (IMAC XXIII)*, Orlando, Florida, 2005.

[3] Matthew S. Allen and Jerry H. Ginsberg, "A global, single-input-multi-output (SIMO) implementation of the algorithm of mode isolation and applications to analytical and experimental data," *Mechanical Systems and Signal Processing*, vol. Submitted, 2005.
[4] Matthew S. Allen and Jerry H. Ginsberg, "A linear least-squares version of the algorithm of mode isolation for identifying modal properties. part II: Application and assessment," *Journal of the Acoustical Society of America (JASA)*, vol. 116, no. 2, pp. 608–615, 2004.
[5] S. Marchesiello, B.A.D. Piombo, and S. Sorrentino, "Application of the CVA-BR method to the Z24 bridge vibration data," in *19th International Modal Analysis Conference (IMAC XIX)*, Kissimmee, Florida, 2001.
[6] Darby J. Luscher, James M. W. Brownjohn, Hoon Sohn, and Charles R. Farrar, "Modal parameter extraction of Z24 bridge data," in *19th International Modal Analysis Conference (IMAC XIX)*, Kissimmee, Florida, 2001.
[7] Brian Schwarz and Mark Richardson, "Post-processing ambient and forced response bridge data to obtain modal parameters," in *19th International Modal Analysis Conference (IMAC XIX)*, Kissimmee, Florida, 2001.
[8] Bart Peeters, *System Identification and Damage Detection in Civil Engineering*, Ph.d., Katholeike Universiteit Leuven, 2000.
[9] Peter Van Overschee and Bart De Moor, "Continuous-time frequency domain subspace system identification," *Signal Processing*, vol. 52, pp. 179–194, 1996.
[10] Kevin Womack and Jeff Hodson, "System identification of the Z24 swiss bridge," in *19th International Modal Analysis Conference (IMAC XIX)*, Kissimmee, Florida, 2001.
[11] Alessandro Fasana, Luigi Garibaldi, Ermanno Giorcelli, and Donato Sabia, "Z24 bridge dynamic data analysis by time domain methods," in *19th International Modal Analysis Conference (IMAC XIX)*, Kissimmee, Florida, 2001.
[12] Randall J. Allemang, *Vibrations Course Notes*, http://www.sdrl.uc.edu/, Cincinnati, 1999.
[13] R. Pintelon and J. Schoukens, *System Identification: a frequency domain approach*, IEEE Press, Piscataway, NJ, 2001.
[14] *http://www.kuleuven.ac.be/bwm/IMAC/*

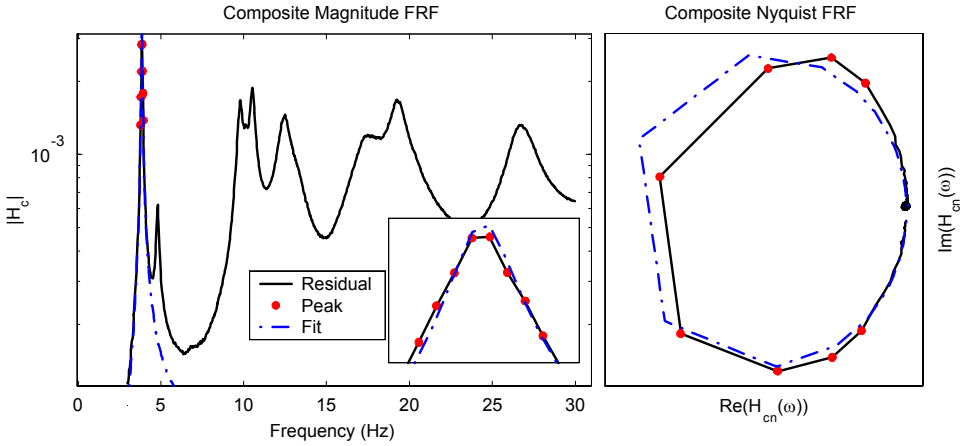

Figure 1: AMI Subtraction Step #1 (single mode fit) for Z24 data. LEFT: Composite Magnitude plots of the residual FRF data (solid) with the peak data highlighted (red dots) and the SDOF fit to the peak (dash-dot). RIGHT: Composite Nyquist plots of the residual (solid) and fit (dash-dot).

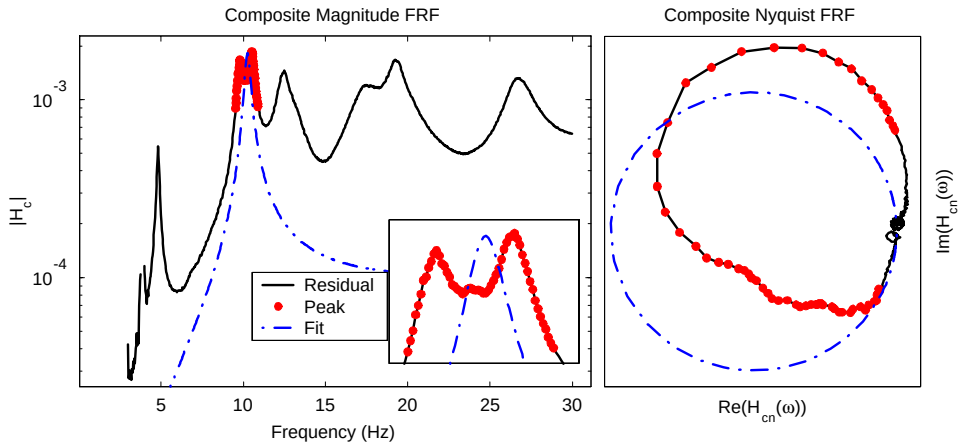

Figure 2: AMI Subtraction Step #2a (single mode fit) for Z24 data. LEFT: Composite Magnitude plots of the residual FRF data (solid) with the peak data highlighted (red dots) and the SDOF fit to the peak (dash-dot). RIGHT: Composite Nyquist plots of the residual (solid) and fit (dash-dot).

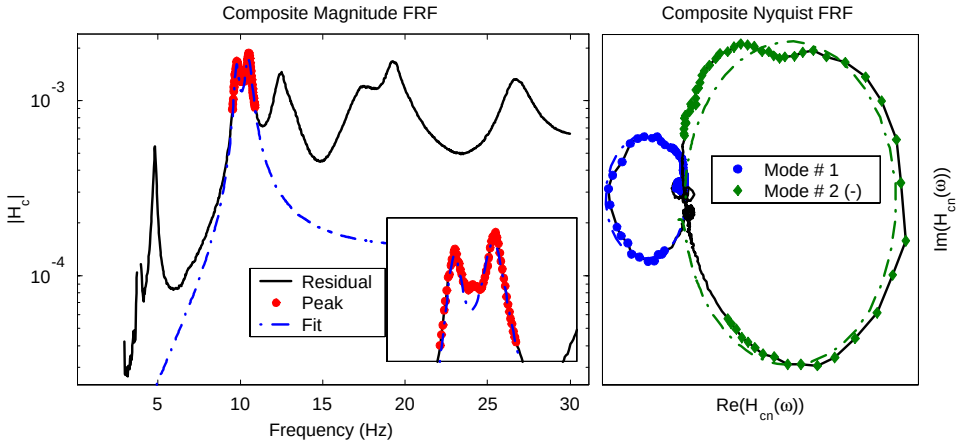

Figure 3: AMI Subtraction Step #2b (two mode fit) for Z24 data. LEFT: Composite Magnitude plots of the residual FRF data (solid) with the peak data highlighted (red dots) and the MDOF fit to the peak (dash-dot). RIGHT: Composite Nyquist plots of the isolation residual (solid) and reconstructed FRF (dash-dot) for each mode.

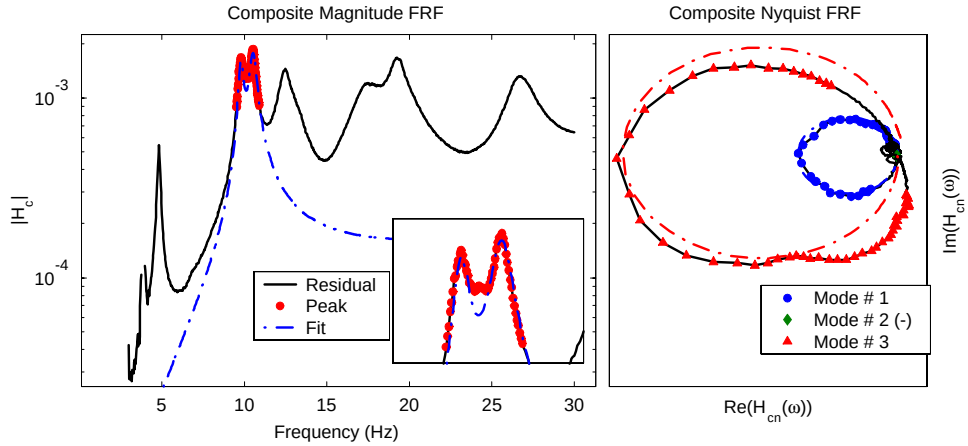

Figure 4: AMI Subtraction Step #2c (three mode fit) for Z24 data. LEFT: Composite Magnitude plots of the residual FRF data (solid) with the peak data highlighted (red dots) and the MDOF fit to the peak (dash-dot). RIGHT: Composite Nyquist plots of the isolation residual (solid) and reconstructed FRF (dash-dot) for each mode.

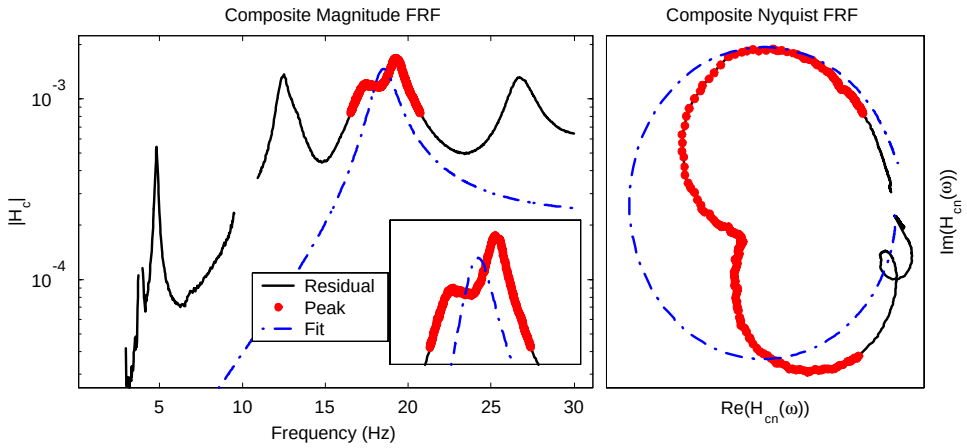

Figure 5: AMI Subtraction Step #3a (single mode fit) for Z24 data. LEFT: Composite Magnitude plots of the residual FRF data (solid) with the peak data highlighted (red dots) and the SDOF fit to the peak (dash-dot). RIGHT: Composite Nyquist plots of the residual (solid) and fit (dash-dot).

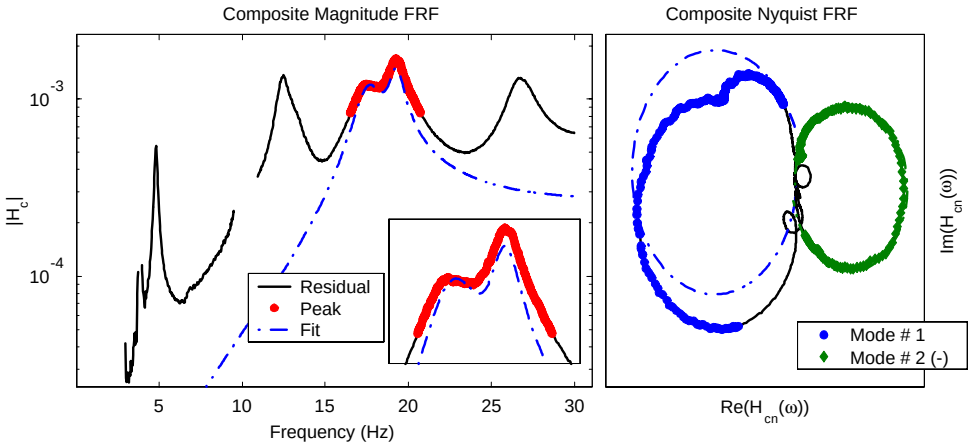

Figure 6: AMI Subtraction Step #3b (two mode fit) for Z24 data. LEFT: Composite Magnitude plots of the residual FRF data (solid) with the peak data highlighted (red dots) and the MDOF fit to the peak (dash-dot). RIGHT: Composite Nyquist plots of the isolation residual (solid) and reconstructed FRF (dash-dot) for each mode.

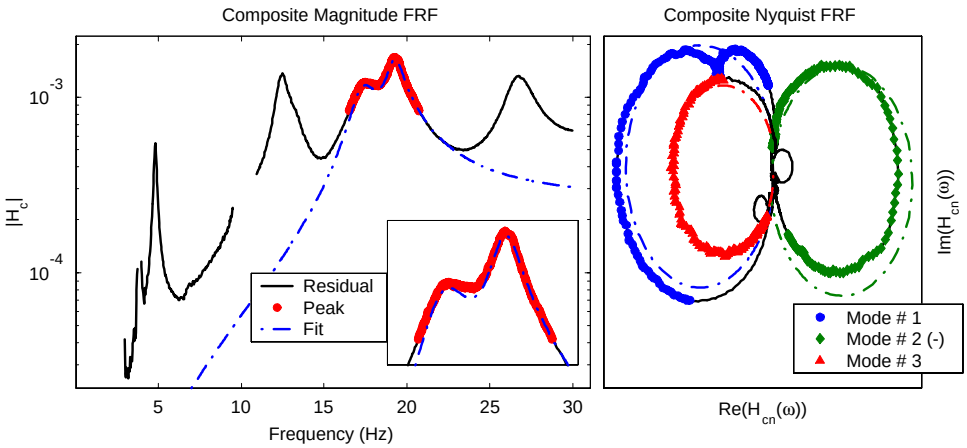

Figure 7: AMI Subtraction Step #3c (three mode fit) for Z24 data. LEFT: Composite Magnitude plots of the residual FRF data (solid) with the peak data highlighted (red dots) and the MDOF fit to the peak (dash-dot). RIGHT: Composite Nyquist plots of the isolation residual (solid) and reconstructed FRF (dash-dot) for each mode.

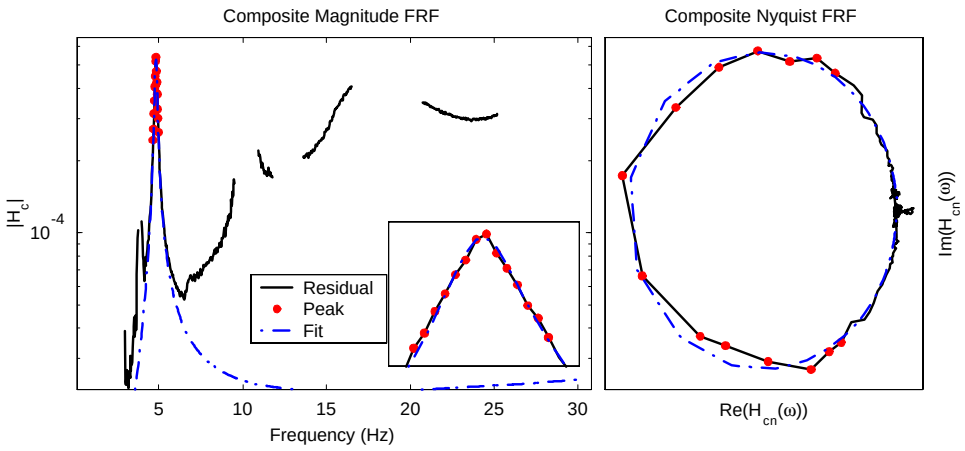

Figure 8: AMI Subtraction Step #6 (single mode fit) for Z24 data. LEFT: Composite Magnitude plots of the residual FRF data (solid) with the peak data highlighted (red dots) and the SDOF fit to the peak (dash-dot). RIGHT: Composite Nyquist plots of the residual (solid) and fit (dash-dot).

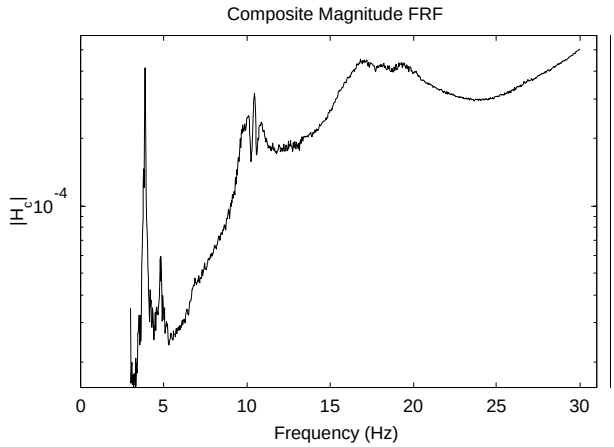

Figure 9: Magnitude composite of the residual FRF data after mode isolation.

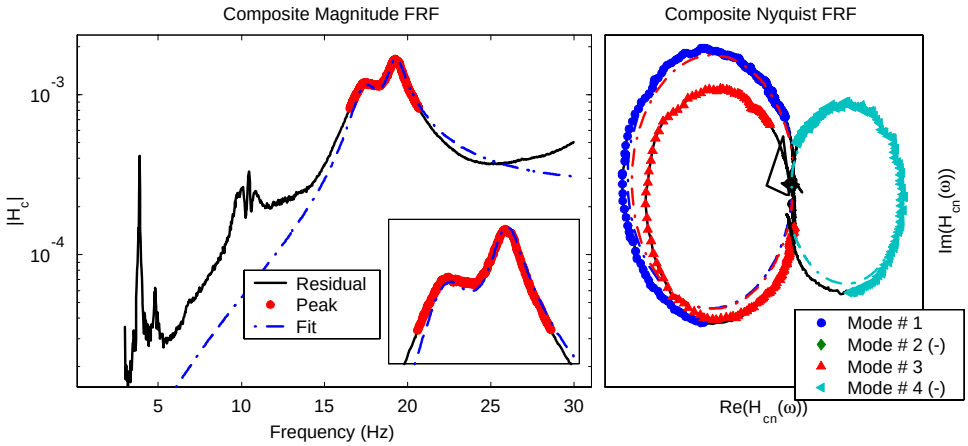

Figure 10: AMI Subtraction Step #7b (four mode fit) for Z24 data. LEFT: Composite Magnitude plots of the residual FRF data (solid) with the peak data highlighted (red dots) and the MDOF fit to the peak (dash-dot). RIGHT: Composite Nyquist plots of the isolation residual (solid) and reconstructed FRF (dash-dot) for each mode.

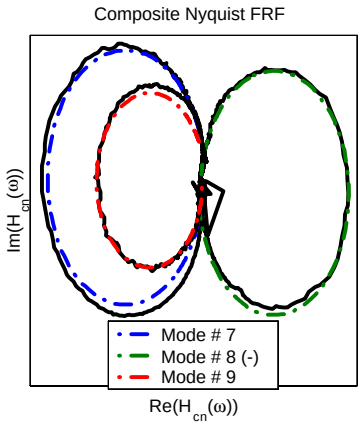

Figure 11: Composite Nyquist plots of the isolated FRFs and the reconstructed FRFs for modes 7-9 after mode isolation and refinement. Each composite Nyquist plot pair was created using the residue matrix for the mode in focus.

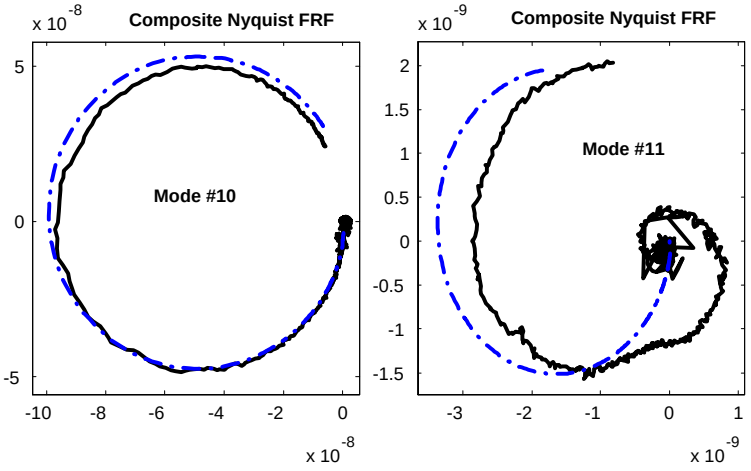

Figure 12: Composite Nyquist plots of the isolated FRFs and the reconstructed FRFs for modes 10 and 11 after mode isolation and refinement. Each composite Nyquist plot pair was created using the residue matrix for the mode in focus.

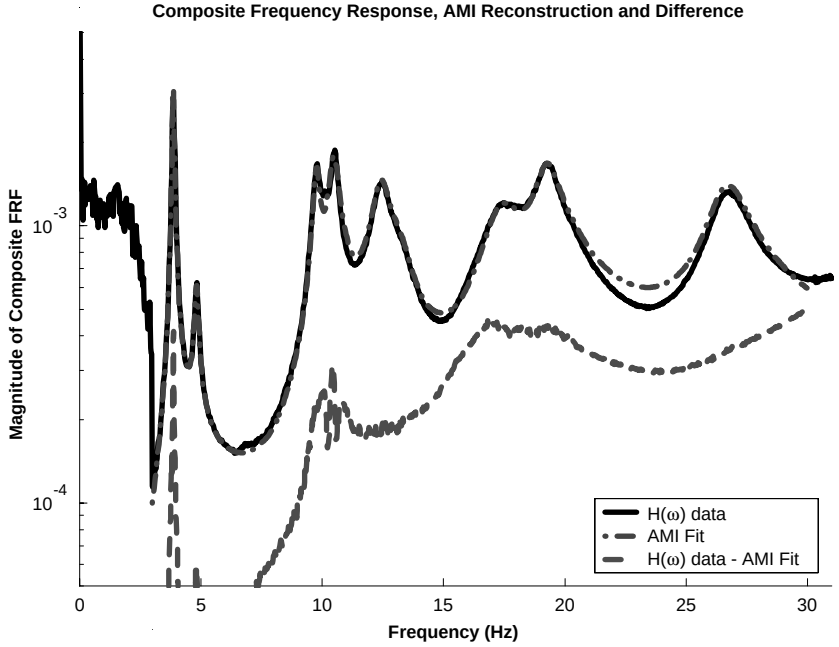

Figure 13: Magnitude composite FRFs of the Z24 data, AMI's recontstruction and the difference between the two.

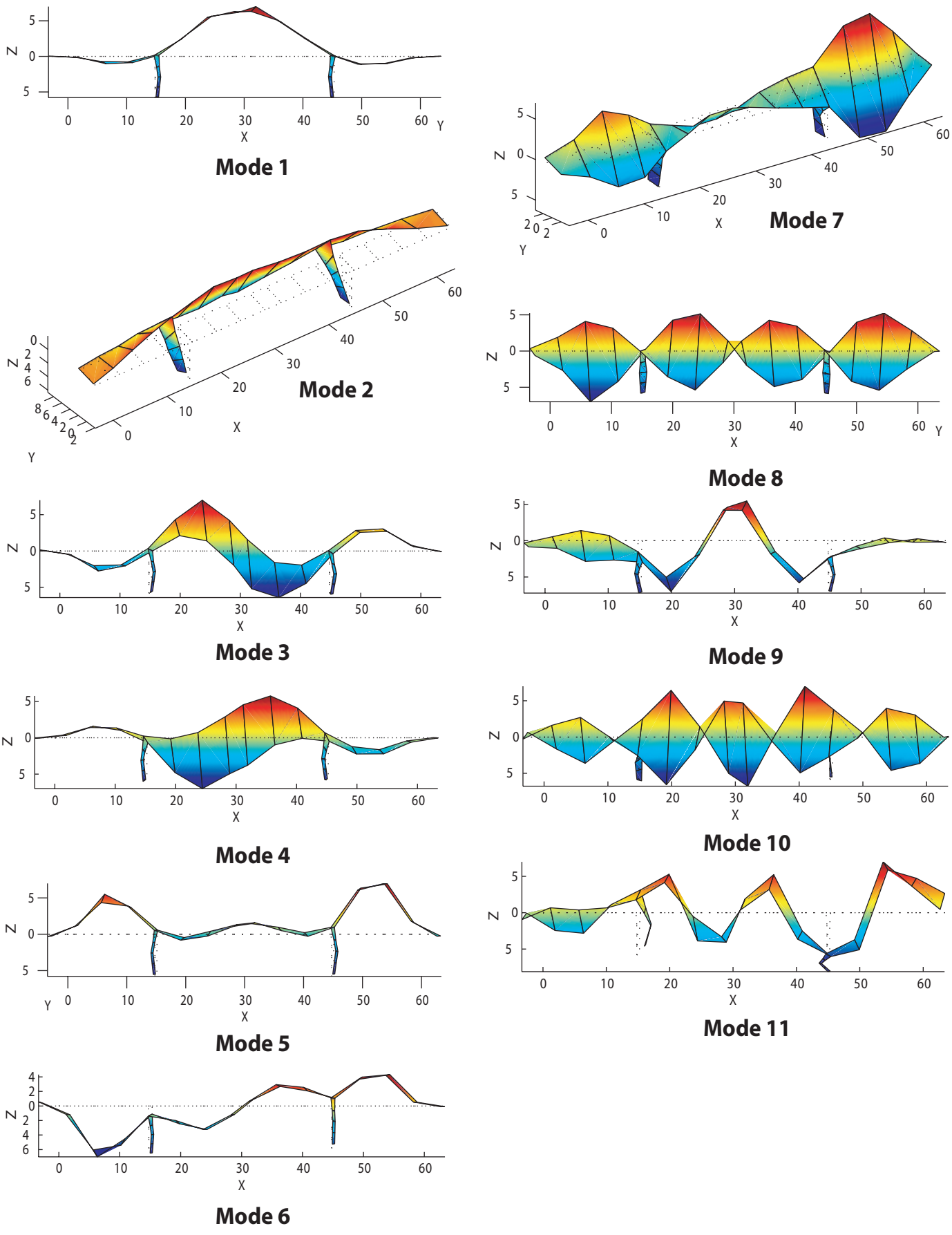

Figure 14: Mode shapes for Z24 from MIMO-AMI. Dotted lines show the undisplaced bridge.